J. Fluid Mech. (2010), *vol.* 651, *pp.* 339–356.
doi:10.1017/S0022112009993983

Experimental investigation of the structure of large- and very-large-scale motions in turbulent pipe flow

SEAN C. C. BAILEY† AND ALEXANDER J. SMITS
Department of Mechanical and Aerospace Engineering, Princeton University, Princeton, NJ 08544 USA

(Received 1 October 2009; revised 8 December 2009; accepted 11 December 2009;
first published online 24 March 2010)

Multi-point velocity measurements have been performed in turbulent pipe flow at $Re_D = 1.5 \times 10^5$ and combined with cross-spectral and proper orthogonal decomposition analysis to elucidate information on the structure of the large- and very-large-scale motions in the outer layer of wall-bounded flows. The results indicate that in the outer layer the large-scale motions (LSM) may be composed of detached eddies with a wide range of azimuthal scales, whereas in the logarithmic layer they are attached. The very-large-scale motions (VLSM) have large radial scales, are concentrated around a single azimuthal mode and make a smaller angle with the wall compared to the LSM. The results support a hypothesis that only the detached LSM in the outer layer align to form the VLSM.

1. Introduction

Recent flow visualizations, numerical studies and particle image velocimetry investigations have revealed the existence of large- and very-large-scale motions in wall-flows. Large-scale motions (LSM) (Kim & Adrian 1999; Guala, Hommema & Adrian 2006; Balakumar & Adrian 2007) are believed to be created by the vortex packets formed when multiple hairpin structures travel at the same convective velocity (Zhou *et al.* 1999). A characteristic feature of the LSM is that the hairpin structures within the packet align in the streamwise direction and induce regions of low streamwise momentum between the legs of the hairpin vortices (Adrian, Meinhart & Tomkins 2000; Ganapathisubramani, Longmire & Marusic 2003; Tomkins & Adrian 2003; Hutchins, Hambleton & Marusic 2005). The LSM have a streamwise scale of approximately 2–3 times the wall layer thickness and have been associated with the occurrence of bulges of turbulent fluid at the edge of the wall layer. A thorough review of the evidence supporting the existence of hairpin vortices and their organization into packets is provided by Adrian (2007).

Meandering, low streamwise momentum fluid flanked by narrow regions of higher momentum fluid has also been observed in the logarithmic and wake regions of wall-flows (Kim & Adrian 1999; Tomkins & Adrian 2005; Guala *et al.* 2006; Balakumar & Adrian 2007; Hutchins & Marusic 2007*b*; Monty *et al.* 2007). In internal flows, the motions are typically referred to as very-large-scale motions (VLSM), whereas in external flows they are more commonly referred to as 'superstructures'. Both VLSM

† Present address: Department of Mechanical Engineering, University of Kentucky, Lexington, KY 40506, USA. Email address for correspondence: scbailey@engr.uky.edu

and superstructures have been found to be much longer than the sublayer streaks and scale on outer variables rather than inner variables. Although the spanwise/azimuthal meandering of these regions makes it difficult to determine their typical streamwise extent, hot-wire rake measurements in channels and pipes (Monty *et al.* 2007) have found instances of VLSM in internal flows as long as 20 times the channel half-height or pipe radius, while similar experiments in boundary layers (Hutchins & Marusic 2007*b*) show that the superstructures tend to be shorter, with a typical length of about 6 times the boundary layer thickness (as inferred from frequency spectra). In addition, Monty *et al.* (2009) note that the superstructures in boundary layers appear to be limited to the logarithmic region, whereas for internal geometries the VLSM are found to persist well into the outer layer. In contrast, Tutkun *et al.* (2009) found evidence of weak elongated structures within boundary layers out to the edge of the layer. The origin of the VLSM and superstructures is not yet clear. Kim & Adrian (1999) proposed that the VLSM are caused by pseudo-streamwise alignment of the LSM, whereas Del Álamo & Jiménez (2006) suggested they could be formed by linear or nonlinear instabilities.

Spectral analysis of the large- and very-large-scale motions indicates that they make a non-negligible contribution to the turbulent kinetic energy and Reynolds stress production (Guala *et al.* 2006; Balakumar & Adrian 2007), which distinguishes them from the inactive motions proposed by Townsend (1976). A careful analysis of DNS data has also revealed the footprint of the outer-scaled motions within the inner-scaled inner layer (Hoyas & Jiménez 2006; Hutchins & Marusic 2007*a*,*b*), and Mathis, Hutchins & Marusic (2009) found modulation of the near wall cycle by long wavelength motions further from the wall, which is supported by the correlations measured by Tutkun *et al.* (2009). These results suggest that motions in the logarithmic and outer layer may have a strong influence on the behaviour of the near-wall turbulence.

The LSM and VLSM have therefore proven to be important features of turbulent wall-flows. To improve our understanding of these flow features, Bailey *et al.* (2008) performed a cross-spectral analysis of the azimuthal scales of LSM and VLSM in pipe flow, and the objective of the current investigation is to build on that work by investigating their wall-normal scales within the logarithmic and wake regions. To this end, multi-point velocity measurements were obtained and analysed using cross-spectral analysis and proper orthogonal decomposition (POD).

2. Experiment description

2.1. *Experimental facility*

The experiments were conducted in the Princeton University/Office of Naval Research Superpipe facility (Zagarola 1996; Zagarola & Smits 1998). The facility consists of a closed return pressure vessel containing a long test pipe downstream of flow conditioning and heat exchanging sections. By driving air compressed at up to 200 atm through the test pipe, fully developed pipe flow is generated over a wide Reynolds number range, from $Re_D = 3.1 \times 10^4$ to 3.5×10^7, where D is the pipe diameter, $\langle U \rangle$ is the area-averaged velocity and ν is the kinematic viscosity.

The current experiments were conducted in a commercial steel pipe with an average inner diameter of 129.84 mm and an overall length of 200 D. The interior surface finish of the pipe has a root mean square roughness height of $k_{rms} = 5\,\mu$m and an equivalent sand grain roughness of $k_s \simeq 1.6\,k_{rms}$. Further details of this test pipe, including mean

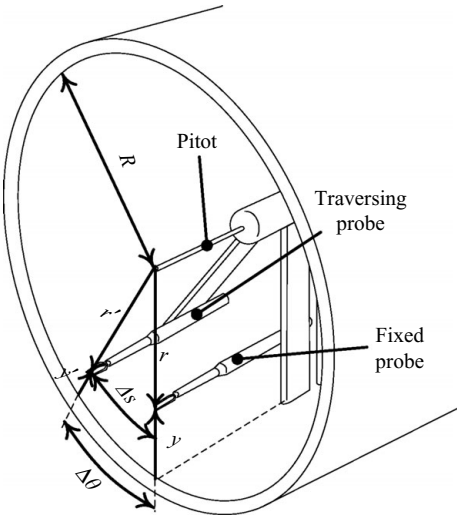

FIGURE 1. Sketch illustrating experimental geometry and nomenclature.

flow measurements and surface profilometry are given by Langelandsvik, Kunkel & Smits (2008).

2.2. *Instrumentation*

Measurements were performed using two single-sensor hot-wire probes with tungsten wires of 2.5 μm diameter and 0.5 mm sensing length. Both probes were mounted on a traversing system positioned 196 D downstream of the pipe inlet, with the probe sensors aligned in the wall-normal direction. The traversing system was designed such that a single probe, used as a reference probe, could be positioned at a fixed wall-normal distance r from the probe centreline while a second traversing probe could be positioned at a radial location r', with radial separation between the two probes of Δr. The traversing probe could be rotated azimuthally to an arbitrary angular separation $\Delta\theta$ with respect to the reference probe. The traversing probe was driven at a 1:1 gear ratio by a high resolution stepper motor, located outside the test pipe and operated in micro-step mode, resulting in an angular positioning resolution of $\pm 0.0018^{\circ}$. The traverse geometry is illustrated in figure 1. Also shown are the orientations of the radial and wall-normal positions of the fixed and traversing probes, the angular separation, $\Delta\theta$, and azimuthal separation distance, $\Delta s = r'\Delta\theta$. The effect of probe blockage and asymmetry of the traverse path introduced by the traverse was evaluated by Bailey *et al.* (2008).

The frequency response of both probes was always greater than 70 kHz. The anemometer output was filtered at 10 kHz (fourth-order Butterworth filter) and digitized at 20 kHz for 180 s long samples using a 16-bit simultaneous sample and hold A/D board (National Instruments PCI-6123).

The test pipe was instrumented with 21 pressure taps, separated by 165.1 mm in the streamwise direction and connected through a 40 port pressure scanner to a 133.3 Pa (1 Torr) pressure transducer. These taps were used to determine the streamwise pressure gradient and hence the friction velocity, $u_\tau = \sqrt{(-\mathrm{d}p/\mathrm{d}x)D/4\varrho}$, where ϱ is the air density.

Probe calibration was performed *in situ* before each measurement run using a Pitot probe located at the pipe centreline. During calibration, the centreline velocity, U_{cl},

and friction velocity were measured. The mean velocity at the probe radial position was then found using the outer-scaled velocity profile data of Langelandsvik *et al.* (2008). As the outer scaling is relatively insensitive to Reynolds number for $y/R > 0.07$, and calibrations needed to be performed over only a relatively narrow velocity range (corresponding to Re_D between approximately 1×10^5 and 2×10^5), this technique provided an accurate relationship between mean centreline velocity and mean velocity at the probe measurement position. For example, the values of $(U - U_{cl})/u_\tau$, in the range $0.1 < y/R < 0.5$, measured by McKeon *et al.* (2004) and Langelandsvik *et al.* (2008) at $Re_D = 7.5 \times 10^4$ and 2.2×10^5 differed from Langelandsvik *et al*'s values for $Re_D = 1.5 \times 10^5$ by only 2.5 % to 5 %.

After correcting the measured bridge voltage for temperature changes (typically less than 0.5°C) using the correction described in Tavoularis (2005), a least-squares fit of the calibration data to King's law (with an exponent of 0.45) was used to determine the velocity measured by the probe, $U^+(t) = U(t)/u_\tau$. This calibration technique yielded first-order statistics that were all within 3 % of values previously measured in the same facility and second-order statistics within 6 %.

2.3. *Measurement conditions*

Using the Reynolds number independence in azimuthal scale observed by Bailey *et al.* (2008) as a guide, measurements were performed at a single Reynolds number of 1.5×10^5, corresponding to the hydraulically smooth flow regime (Langelandsvik *et al.* 2008). At this Reynolds number, the measured friction velocity was 0.8 m s^{-1}, resulting in $Re_\tau = Ru_\tau/\nu$ of 3.4×10^3, viscous length $\nu/u_\tau = 20\,\mu$m, and $k_s^+ = k_s u_\tau/\nu = 0.4$.

Measurement positions were selected to allow POD of the velocity field following Tutkun, Johansson & George (2008). Data were taken at five wall-normal stations located $0.1R$, $0.2R$, $0.3R$, $0.4R$ and $0.5R$ from the wall, with fixed probe wall-normal distance denoted by y and traversing probe distance denoted by y' (corresponding to radial positions r and r'). The results of Langelandsvik *et al.* (2008) indicate that these measurement positions are within the logarithmic layer at $0.1R$ and extend into the wake region with the upper edge of the logarithmic region around $0.2R$. For each y/R position of the fixed probe, measurements were performed with the traversing probe at all five y'/R stations with the probe traversed unidirectionally from $\Delta\theta = 5°$ to $\Delta\theta = 180°$ at 5° increments for each y'/R location. Additional measurements were made at $\Delta\theta = 0°$ to complete the mapping of the measurement region from $0.1R$ to $0.5R$ from the wall and $\Delta\theta = 0°$ to $\Delta\theta = 180°$ for each y/R position of the fixed probe. Symmetry conditions were used to extend this mapping from $\Delta\theta = 180°$ to 360°, since measurements performed with the reference probe at r separated by $\Delta\theta$ from the traversing probe at r' were equivalent to the measurements made with the reference probe at r' separated from the traversing probe at r by $-\Delta\theta$.

3. Results and discussion

3.1. *Autospectra*

The pre-multiplied autospectrum calculated from the fixed reference probe is shown in figure 2 for each measured wall-normal position. The contributions by the LSM and VLSM to the energy are evident as localized peaks in the autospectra, indicated by dashed lines in figure 2. Guala *et al.* (2006) found that the VLSM occur at $2\pi f R/\overline{U} < 2$ and LSM at $2\pi f R/\overline{U} > 2$, whereas from figure 2 VLSM occurring at <1 and LSM >1 would appear more appropriate. Guala *et al.* (2006) determined their wavenumber range by examining spectra from as close to the wall as $y/R = 0.05$, so this difference

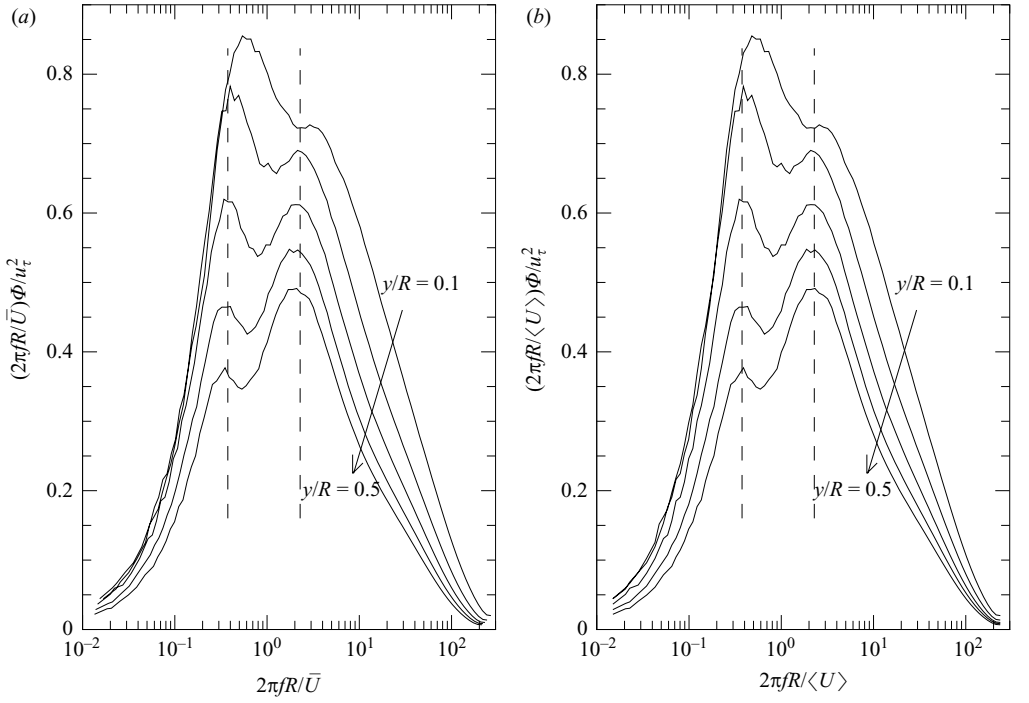

FIGURE 2. Pre-multiplied autospectra measured by fixed probe at different wall-normal positions with wavenumber calculated using (*a*) local mean velocity and (*b*) area-averaged velocity.

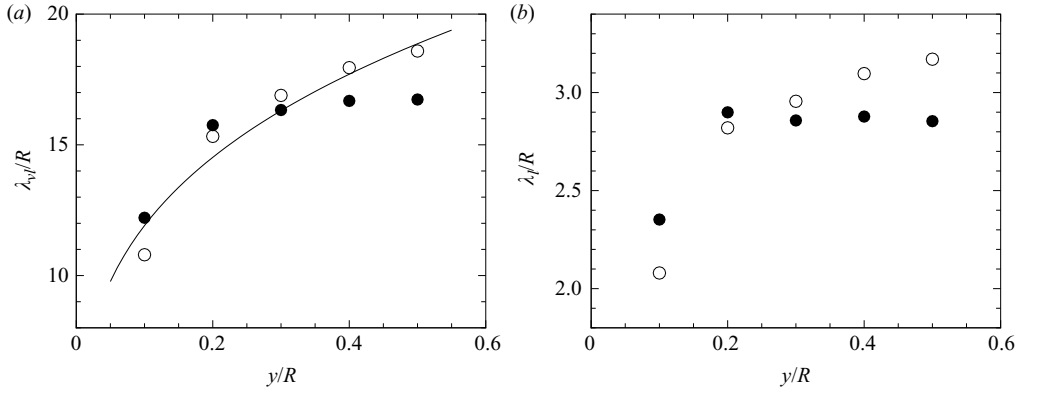

FIGURE 3. Estimate of wavelength of (*a*) VLSM and (*b*) LSM as determined from corresponding peak in pre-multiplied autospectra. Hollow symbols show wavelength estimated using local mean for convection velocity, solid symbols use area-averaged velocity. The line is power law of Monty *et al.* (2009) for VLSM wavelength.

in selected wavenumber range for each motion is most likely explained by the growth of both VLSM and LSM wavelengths with increased distance from the wall.

In figure 2(*a*), the streamwise wavenumber is estimated from frequency f by Taylor's hypothesis using the local mean velocity, as $2\pi f/\overline{U}$, whereas in figure 2(*b*) the streamwise wavenumber is estimated using the area-averaged velocity, as $2\pi f/\langle U\rangle$. The wavelengths corresponding to the peaks in the autospectra are shown in figure 3

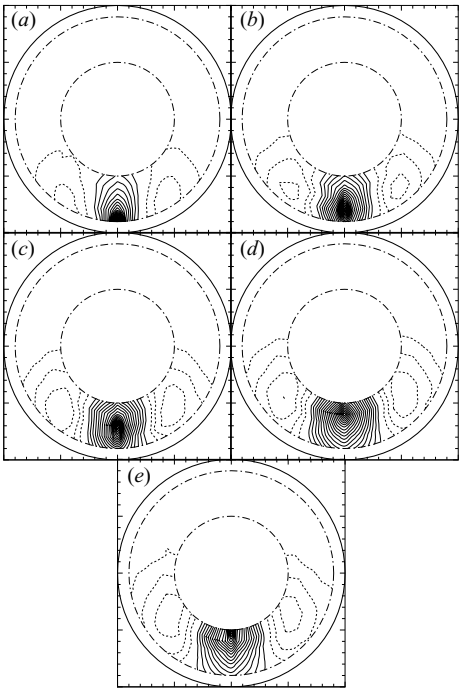

FIGURE 4. Correlation coefficient, $\rho(r, r', \Delta\theta, 0)/\rho(r, r, 0, 0)$, across measurement plane with reference probe at (*a*) $y/R = 0.1$, (*b*) $y/R = 0.2$, (*c*) $y/R = 0.3$, (*d*) $y/R = 0.4$ and (*e*) $y/R = 0.5$. Contour spacing is 0.05 with negative values indicated by dashed lines; contour lines at zero are not shown for clarity. Dash-dotted lines delineate measurement extent.

for both the VLSM and LSM peaks. When the local mean velocity is used as an estimate of the local convection velocity, the VLSM wavelength is well represented by the power law of Monty *et al.* (2009):

$$\frac{\lambda_{vl}}{R} = 23\left(\frac{y}{R}\right)^{2/7}. \tag{3.1}$$

However, when the wavelength is estimated using $\langle U \rangle$, the wavelengths of VLSM and LSM remain approximately constant for $y/R > 0.2$ at approximately $16R$ and $2.9R$, respectively. This result supports the notion that the peaks at different wall-normal positions correspond to the same coherent motions (which would be expected to travel at the same convection velocity). The actual streamwise wavenumber of these motions, however, cannot be estimated from these figures because the mean convection velocity for each of these motions is unknown. Finding this convection velocity is not a trivial task, but it is important because the validity of Taylor's hypothesis decreases as the wavelength of the motions increases (cf. Dennis & Nickels 2008).

3.2. *Cross-correlation*

The cross-correlation measured between the two signals was calculated according to

$$\rho(r, r', \Delta\theta, \tau) = \overline{u^+(r, r, 0, t)u^+(r, r', \Delta\theta, t + \tau)}, \tag{3.2}$$

where the overbar indicates a time average, r is the radial position of the reference probe, r' is the radial position of the traversing probe and $u^+ = U^+ - \overline{U^+}$. For $\Delta\theta > 180^\circ$, symmetry conditions give $\rho(r, r', \Delta\theta, \tau) = \rho(r', r, -\Delta\theta, -\tau)$.

Figure 4 shows a contour map of the correlation in the cross-stream measurement plane at $\tau = 0$ for each of the five reference probe wall-normal positions, normalized

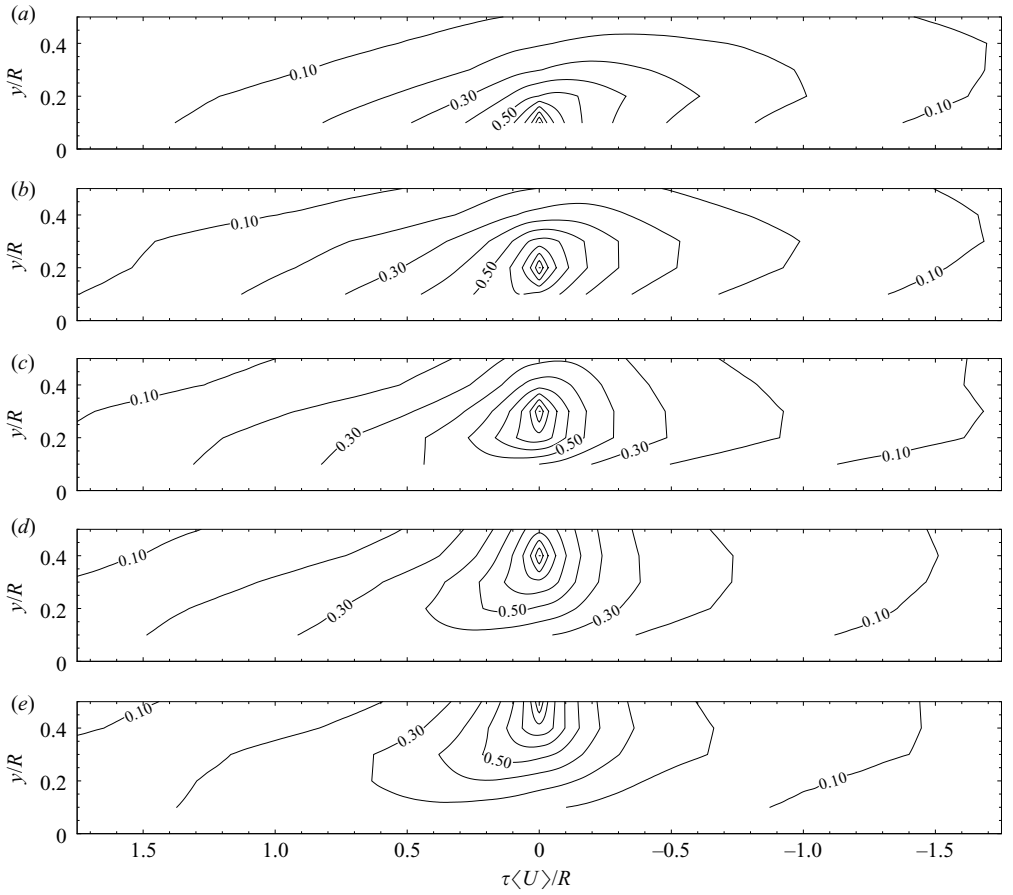

FIGURE 5. Correlation coefficient $\rho(r, r', 0, \tau)/\rho(r, r, 0, 0)$, in wall-normal direction as a function of time-lag when reference probe is at (*a*) $y/R = 0.5$, (*b*) $y/R = 0.4$, (*c*) $y/R = 0.3$, (*d*) $y/R = 0.2$ and (*e*) $y/R = 0.1$.

by the variance measured by the reference probe, $\rho(r, r, 0, 0)$. The profiles of the correlation coefficient at $\Delta r = 0$ (when both probes are on the same azimuthal plane) are consistent with those previously reported for pipe, channel and boundary layer flows (Monty *et al.* 2007; Bailey *et al.* 2008), and the characteristic region of negative correlation is attributed to the presence of coherent motions. Figure 4 clearly illustrates the large spatial scale of the coherent motions, underscoring their importance in the structure of the turbulence. It is also interesting to note that there is no apparent correlation observed within the range $|\Delta\theta > 90°|$, suggesting that these structures are not periodic in the azimuthal direction and that minimal interactions occur between motions on opposite sides of the pipe.

An estimate of the angle of inclination of the coherent motions can be found by examining the planes of $\rho(r, r', 0, \tau)/\rho(r, r, 0, 0)$ at different values of r, where a coarse estimate of the streamwise scale can be found using Taylor's hypothesis with a convection velocity of $\langle U \rangle$. These planes, shown in figure 5, show that the local inclination angle depends on wall-normal position of the reference probe. As the reference position moves away from the wall, the inclination changes between 22° and 80°, depending on Δr and τ. These angles and their variation with wall distance are within the ranges observed for hairpin packet growth angle (Adrian

2007) and previous correlation results (cf. Favre, Gaviglio & Dumas 1957, 1958; Kovasznay, Kibens & Blackwelder 1970; Alving, Smits & Watmuff 1990; Tutkun *et al.* 2009). However, as discussed by Marusic & Heuer (2007), a structure angle can be defined using a reference position at the wall, resulting in a Δr and Reynolds number independent angle of approximately 15° for boundary layers. In the current study, the structure angle is estimated using the correlation with the reference probe located at the nearest point to the wall ($y/R = 0.1$), resulting in an estimated angle of approximately 20° relative to the wall.

3.3. *Spectral filtering*

Cross-correlation results, such as those presented above, are time-averaged quantities and therefore contain contributions from both VLSM and LSM. To investigate the contributions from each type of motion, we note that the cross-correlation can be written as

$$\rho(r, r', \Delta\theta, \tau) = \int_0^\infty [C(r, r', \Delta\theta)\cos(2\pi f\tau) + Q(r, r', \Delta\theta)\sin(2\pi f\tau)]\,\mathrm{d}f, \qquad (3.3)$$

where $C(r, r', \Delta\theta)$ and $Q(r, r', \Delta\theta)$ are the real and imaginary components of the cross-spectrum, respectively (Bendat & Piersol 2000). Hence, it becomes possible to estimate the contribution to the cross-correlation from specific frequency or wavenumber ranges. With reference to figure 2, the contribution from the VLSM, ρ_{vl}, was estimated by calculating ρ from 3.3) within the range $2\pi f R/\langle U\rangle < 1$. Similarly, the contribution from the LSM, ρ_{vl}, was estimated by repeating the calculation over the range $1 < 2\pi f R/\langle U\rangle < 10$. These cutoff wavenumber values were selected based on the POD results discussed in § 3.4, whereby the low wavenumber value was selected to be at the valley between the VLSM and LSM peaks and the high wavenumber cutoff being an upper bound of wavenumbers containing energy from the LSM. This definition differs slightly from that used by Guala *et al.* (2006), who considered all contributions from wavenumbers $2\pi f R/\overline{U} > 2$ to be from the LSM (the effects of choosing different cutoff values is investigated below).

Figure 6 shows isocontours of ρ_{vl} and ρ_l within the transverse measurement plane for $\tau = 0$. Although the abrupt cutoff incurred as a result of the spectral filtering will cause longer LSM to contribute to ρ_{vl} and shorter VLSM to contribute to ρ_l, the results are expected to provide a broad estimate of the average transverse scale of each type of motion. In this figure ρ_{vl} and ρ_l are shown normalized by $\rho(r, r, 0, 0)$, the integral of the entire auto-spectrum measured by the reference probe. Hence, this normalization provides an estimate of the relative energy contained in the VLSM and LSM at the reference probe location. Although the magnitudes of ρ_{vl} and ρ_l are similar, the larger scale of the VLSM causes these motions to dominate the cross-correlation.

When the reference probe is located far from the wall, the LSM appear to have little or no correlation with the motions near the wall, suggesting that in the outer layer these motions are 'detached' from the wall. Here we use the term 'detached to indicate simply that the correlations no longer extend all the way to the wall, and that the motions making up the correlation no longer scale with the distance to the wall, Hence, there are at least two types of LSM: those that are attached to the wall, and those that are detached from the wall.

When the reference probe is located near the wall, there are significant differences in the transverse scale of the VLSM and LSM, which supports the suggestion made by Bailey *et al.* (2008) that the VLSM are not necessarily formed by the streamwise

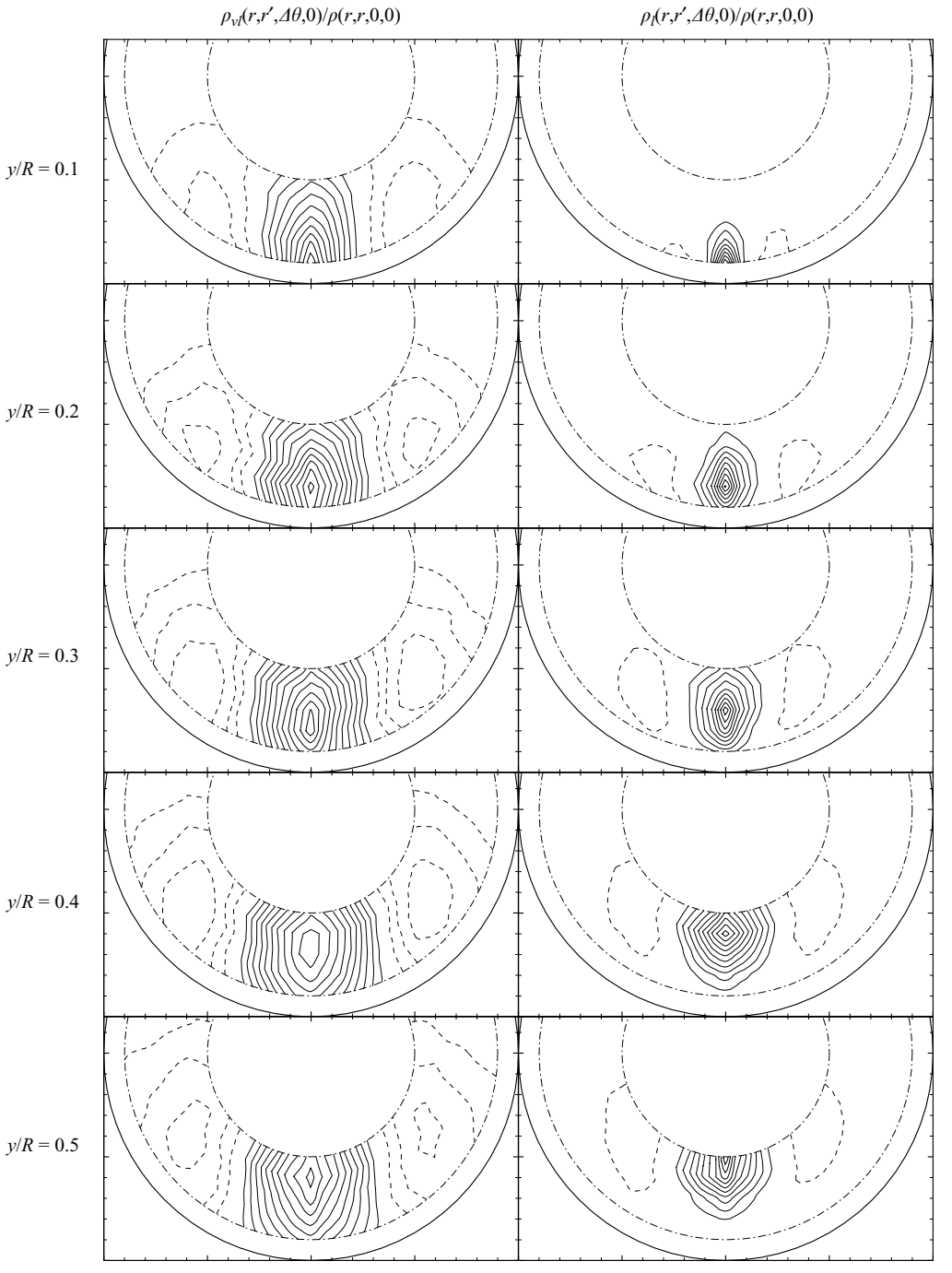

FIGURE 6. Estimates of $\rho_{vl}(r, r', \Delta\theta, 0)$ and $\rho_{l}(r, r', \Delta\theta, 0)$ normalized by $\rho(r, r, 0, 0)$ with reference probe at different wall-normal positions. Contour spacing is 0.04 with negative values indicated by dashed lines and contour at zero removed for clarity.

alignment of the LSM that occur near the wall. However, the azimuthal scale of the LSM when the reference probe is located at $y/R = 0.5$ (figure 6*e*), is of the same order of the azimuthal scale of the VLSM observed when the reference is at $y/R = 0.1$

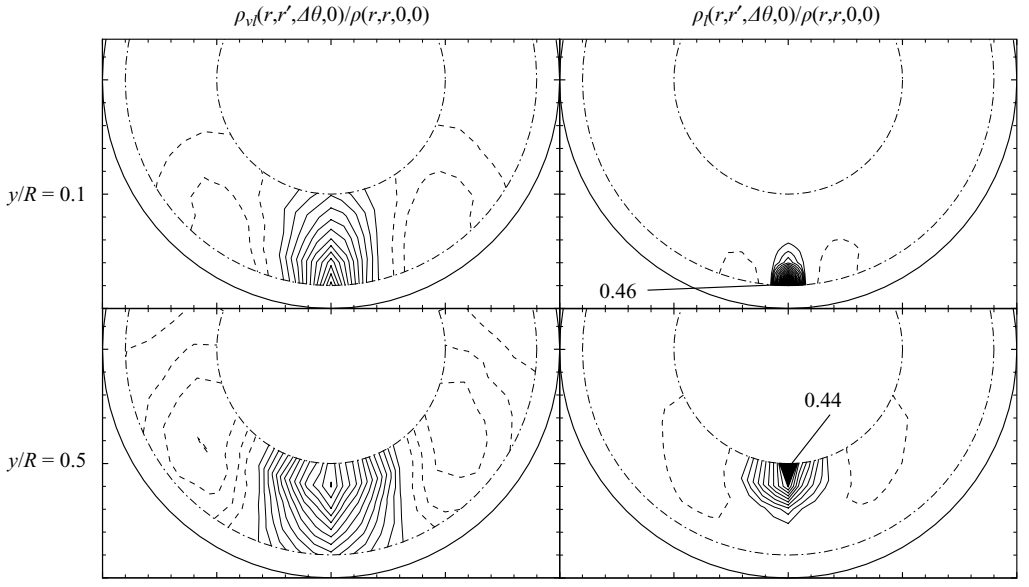

FIGURE 7. Estimates of $\rho_{vl}(r, r', \Delta\theta, 0)$ and $\rho_l(r, r', \Delta\theta, 0)$ normalized by $\rho(r, r, 0, 0)$ using the wavenumber ranges for VLSM and LSM proposed by Guala *et al.* (2006). For ρ_{vl} the contour spacing is 0.04 whereas for ρ_l the contour spacing is 0.02. Negative values indicated by dashed lines and contour at zero removed for clarity.

(figure 6*a*), which means that the VLSM could form from pseudo-alignment of larger, older, detached LSM rather than the smaller LSM located near the wall. Note that the correlations reflect only the average scale of each type of motion and that individual LSM near the wall could have an azimuthal scale comparable to that of the VLSM and align to form the VLSM or, alternatively, the alignment process could widen the LSM involved.

To assess the influence of the spectral filter ranges, the filtering was repeated using the cutoff values proposed by Guala *et al.* (2006), where ρ_{vl} is estimated by integrating the cross-spectrum up to $2\pi f R/\overline{U} = 2$ and ρ_l is estimated by integrating over the remaining wavenumbers. The results are shown in figure 7 for the reference probe at $y/R = 0.1$ and 0.5. When compared to the results in figure 6, it is apparent that the magnitudes of ρ_{vl} and ρ_l are affected by changing the filter ranges, but the spatial scale of the correlations remain largely unaffected.

Isocontours of ρ_{vl} and ρ_l in the streamwise–wall-normal plane are shown in figures 8 and 9 respectively. Comparing these figures reveals clear differences between the VLSM and LSM. Most striking is the presence of negatively correlated regions upstream and downstream of the LSM, which are not evident for the VLSM. The distance between the negatively correlated regions suggests a streamwise length scale of the LSM between 1–2R. Note that regions of $\tau \langle U \rangle / R$ in the range ± 10 were inspected but are not shown on figures 8 and 9 for clarity.

An estimate for the differences in the structure angle of each type of motion can be found using the time lag, τ_{max}, at which the maximum value of ρ_{vl} and ρ_l occurs for each Δr when $\Delta\theta = 0$ and the reference probe is at $y/R = 0.1$. The results are shown in figure 10. When area-averaged velocity is used as a convection velocity, the VLSM structure angle appears to be approximately 14°, much smaller than that of the LSM which is closer to 24°. One potential explanation for this difference might be found in

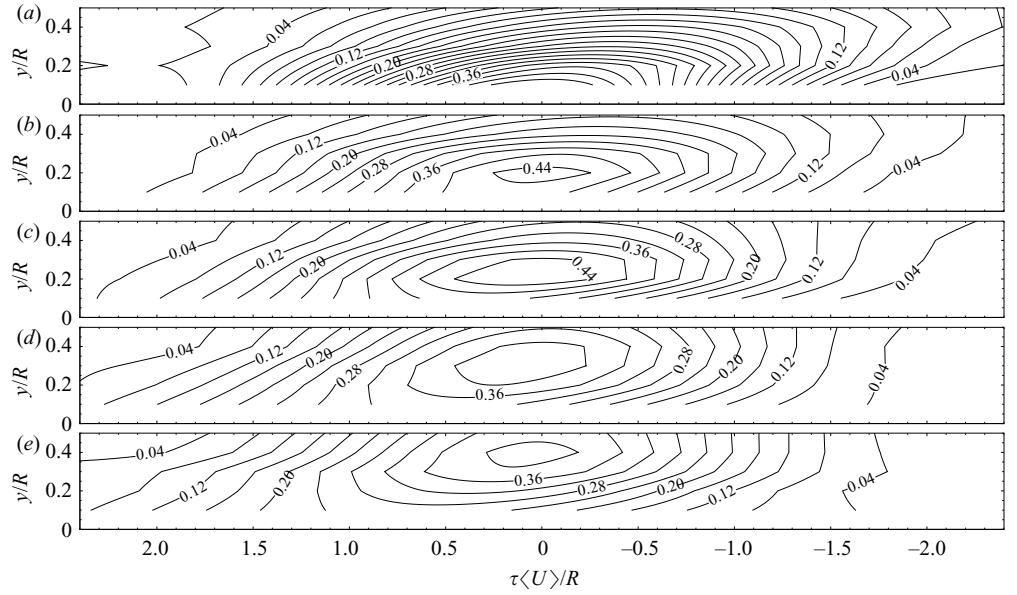

FIGURE 8. Estimates of $\rho_{vl}(r, r', \Delta\theta, 0)$ normalized by $\rho(r, r, 0, 0)$ with reference probe at (*a*) $y/R = 0.1$, (*b*) $y/R = 0.2$, (*c*) $y/R = 0.3$, (*d*) $y/R = 0.4$ and (*e*) $y/R = 0.5$.

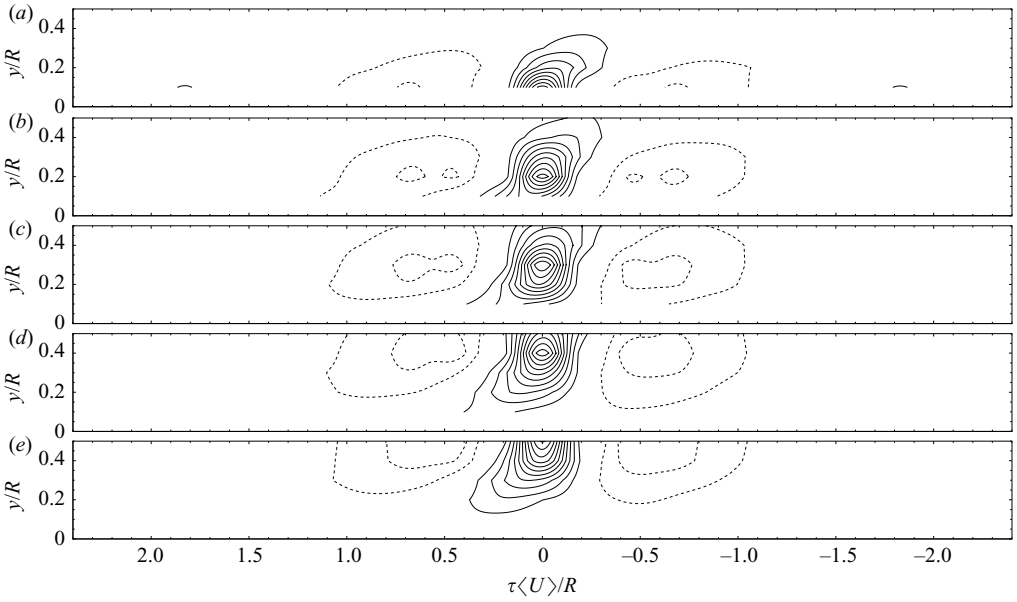

FIGURE 9. Estimates of $\rho_l(r, r', \Delta\theta, 0)$ normalized by $\rho(r, r, 0, 0)$ with reference probe at (*a*) $y/R = 0.1$, (*b*) $y/R = 0.2$, (*c*) $y/R = 0.3$, (*d*) $y/R = 0.4$ and (*e*) $y/R = 0.5$. Contour spacing is 0.04 with negative values indicated by dashed lines; contour lines at zero are removed for clarity.

the earlier observation that within the outer layer the LSM are composed largely of detached eddies, whereas the VLSM extend to the wall. Thus the VLSM are expected to experience higher levels of shear relative to that experienced by the detached LSM.

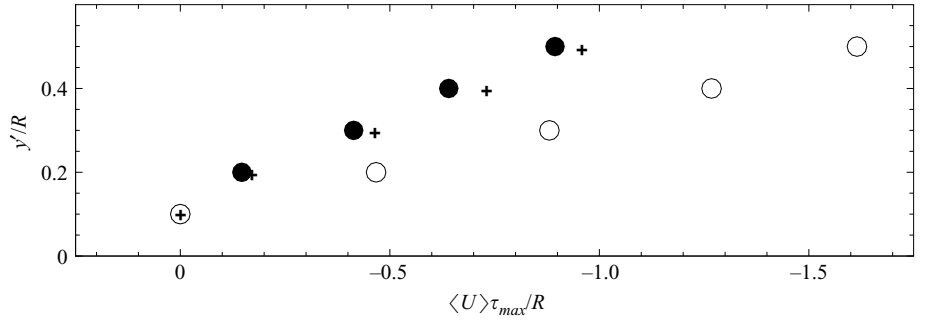

FIGURE 10. Estimated streamwise displacement of peak when reference probe at $y/R = 0.1$ for +, ρ; ○, ρ_{vl}; ● ρ_l.

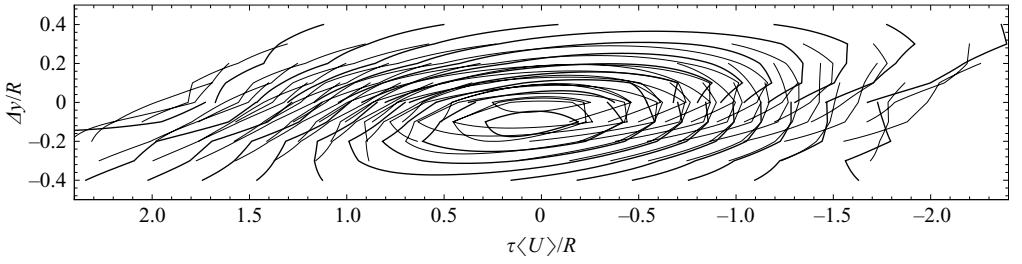

FIGURE 11. Isocontours from figure 8 shown plotted as function of $\Delta y/R$ rather than y/R.

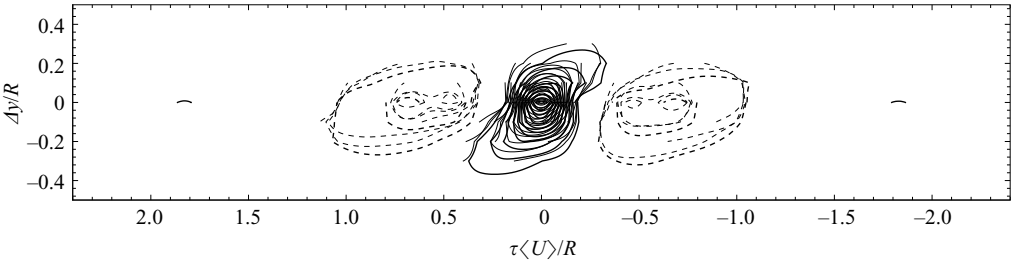

FIGURE 12. Isocontours from figure 9 shown plotted as function of $\Delta y/R$ rather than y/R.

It is also possible, as suggested earlier, that the convection velocities of these two types of motions are different. If we assume that the actual inclination angles of the two motions are approximately the same, then the convection velocity of the LSM needs to be about twice that of the VLSM. This difference in convection velocities may occur if the VLSM are comprised largely of wall-attached eddies and the LSM are composed largely of detached eddies (although a factor of two seems unlikely). In turn, this implies that the streamwise wavenumber spectra would be very different from the autospectra shown in figure 2, underscoring the danger inherent in assuming Taylor's hypothesis for long wavelength motions (Dennis & Nickels 2008). In all likelihood, the differences in streamwise–wall-normal angle observed between figure 10 can be attributed to a combination of both effects, that is, increased shear across the VLSM and differences in convection velocity between the two motions.

The streamwise–wall-normal isocontours of ρ_{vl} and ρ_l shown in figures 8 and 9 reveal a remarkable similarity for different reference probe locations, which is true for both the VLSM and LSM. This similarity is highlighted in figures 11 and 12, where

the contours are collected onto the same plot. This scale-independence suggests the interesting possibility that within the outer layer the streamwise–wall-normal scale of the structures no longer depends on the distance from the wall, in contrast to the behaviour of the azimuthal scale which grows with y. Furthermore, figure 11 indicates that the wall-normal scale of the VLSM is on the order of R, so that these motions are expected to influence behaviour near the wall even when they are near the edge of the wall layer.

3.4. *Proper orthogonal decomposition*

POD analysis provides a means to determine the distribution of energy amongst different modes, and can help to identify the most energetic motions in a flow. Unlike the autospectra, which illustrate the energy distribution at a single point in space, the POD results represent the energy distribution across the entire measurement plane and therefore allow an evaluation of the coherence and importance of the VLSM and LSM within the flow field.

POD was performed following the procedure outlined in Tutkun *et al.* (2008) for azimuthally homogeneous flows, and the procedure will only be briefly summarized here. For consistency, their nomenclature will also be maintained. The POD modes were determined using the following procedure:

(*a*) The cross-spectra between each pair of measurement locations, $\tilde{S}(r, r'; \Delta\theta; f)$ was calculated from the complex conjugate of the Fourier transforms of u^+ measured by the probes at r and r' with angular separation $\Delta\theta$;

(*b*) A Fourier series expansion was performed on $\tilde{S}(r, r'; \Delta\theta; f)$ in the azimuthal direction to determine $S(r, r'; m; f)$, where m is the azimuthal mode;

(*c*) The eigenvalues $\lambda^{(n)}(m; f)$ and eigenspectra $\phi^{(n)}(r; m; f)$ were determined from

$$\int_{r'} W(r, r'; m; f)\hat{\phi}^{*(n)}(r'; m; f)\,\mathrm{d}r' = \hat{\lambda}^{(n)}(m; f)\hat{\phi}^{(n)}(r; m; f) \tag{3.4}$$

where to achieve Hermitian symmetry:

$$W(r, r'; m; f) = r^{1/2}S(r, r'; m; f)r'^{1/2}, \tag{3.5}$$

$$\hat{\phi}^{*(n)} = \phi^{*(n)}(r'; m; f)r'^{1/2}, \tag{3.6}$$

$$\hat{\phi}^{(n)} = r^{1/2}\phi^{(n)}(r'; m; f) \tag{3.7}$$

and

$$\hat{\lambda}^{(n)}(m; f) = \lambda^{(n)}(m; f). \tag{3.8}$$

The analysis produces eigenvalues λ representing the radial mode n, ordered by the most to least energetic, distributed in frequency f and azimuthal Fourier mode m, which are ordered from longest to shortest wavelengths. Furthermore, the cross-spectra $S(r, r'; m; f)$ can be reconstructed from

$$r^{1/2}S(r, r'; m; f)r'^{1/2} = W(r, r'; m; f) = \sum_{n=1}^{N} \lambda^{(n)}\hat{\phi}^{*(n)}(r'; m; f)\hat{\phi}^{(n)}(r; m; f) \tag{3.9}$$

and $\rho(r, r'; \Delta\theta; \tau)$ can be recovered by performing inverse Fourier transforms on $S(r, r'; m; f)$. Thus, POD can also be used as a form of filter by selecting which radial modes, azimuthal modes, and frequencies to use to reconstruct the cross-spectra.

The sum of the streamwise velocity contribution to the kinetic energy within the measurement plane can be recovered by summing the eigenvalues over all frequencies, as well as all azimuthal and radial POD modes, allowing the fraction of kinetic energy

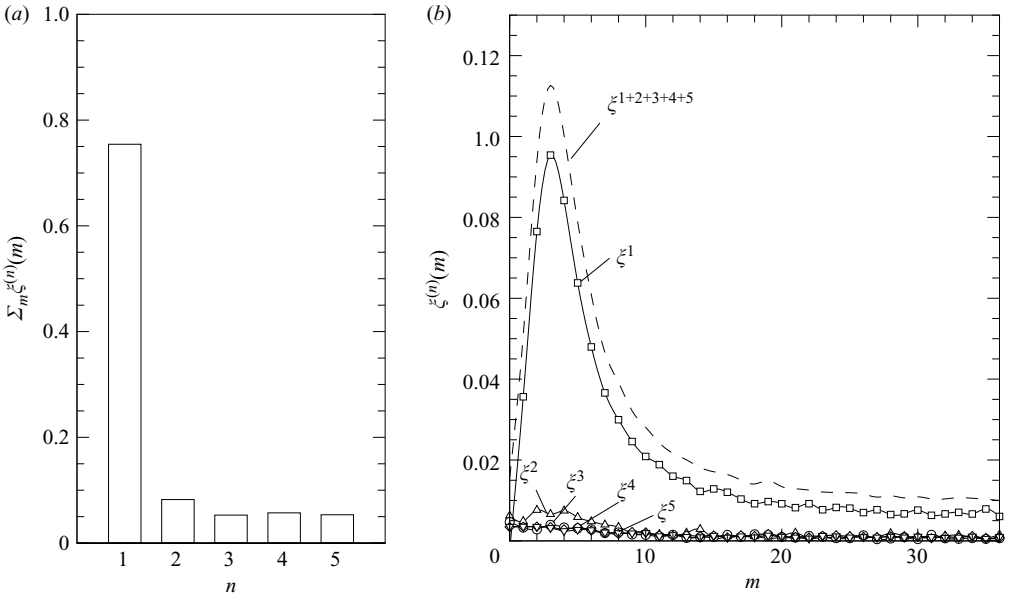

FIGURE 13. Fraction of kinetic energy contained within (*a*) radial and (*b*) azimuthal modes.

contained within an azimuthal and radial mode to be estimated through

$$\xi^{(n)}(m) = \frac{\int_0^\infty \lambda^{(n)}(m, f)\,\mathrm{d}f}{\sum_{m=0}^{M-1}\sum_{n}^{N}\int_0^\infty \lambda^{(n)}(m, f)\,\mathrm{d}f} \tag{3.10}$$

(Tutkun *et al.* 2008) where M is the number of azimuthal modes and N is the number of radial modes.

Figure 13(*a*) shows the energy content contained within each radial mode as determined through $\sum_0^{M-1} \xi^{(n)}(m)$. Approximately 75 % of the energy is contained in radial mode 1. The distribution of energy amongst the azimuthal modes is shown in figure 13(*b*) for each of the radial modes as well as for the sum over all radial modes. Unlike the radial modes, there is no dominant azimuthal mode, with most of the energy contained within the range $m < 20$, concentrated around $m = 3$.

An illustration of the scale of motions contained in $n = 1$, $m = 3$ can be found by applying (3.9) using only these modes. Figure 14 shows the reconstructed correlation map for $\tau = 0$ with the reference probe at $y/R = 0.1$. The results clearly show the similarity in the scale between $n = 1$, $m = 3$ and $\rho_{vl}(r, r', \Delta\theta, 0)$ shown in figure 6.

The distribution of energy within radial mode 1 and azimuthal modes 0 to 20 is illustrated using isocontours of the eigenvalues in figure 15. To better reflect the wavenumbers where the majority of the energy content lies, and to better compare the results to the pre-multiplied autospectra results, the eigenvalues are shown pre-multiplied by the frequency normalized by $2\pi f R/\langle U \rangle$. Also shown in figure 15 are the pre-multiplied autospectra previously shown in figure 2 to allow easy identification of the VLSM and LSM wavenumber ranges.

The results indicate that, in general, motions with wider azimuthal scales have longer wavelengths. In addition, localized peaks in $\lambda^{(1)}$ are evident in azimuthal

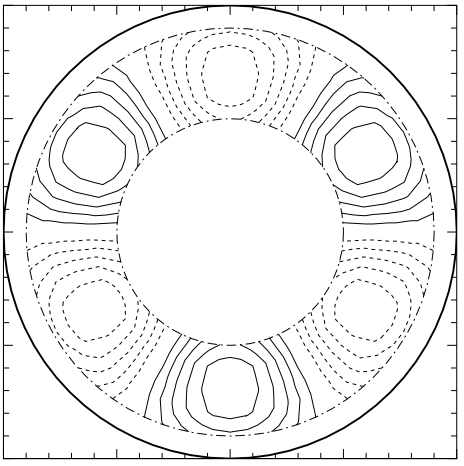

FIGURE 14. Reconstructed correlation map for $n=1$, $m=3$ with the reference probe at $y/R=0.1$ and $\tau=0$, normalized by $\rho(r, r, 0, 0)$. Contour levels at 0.01, with negative values indicated by dashed lines and zero contour not shown for clarity.

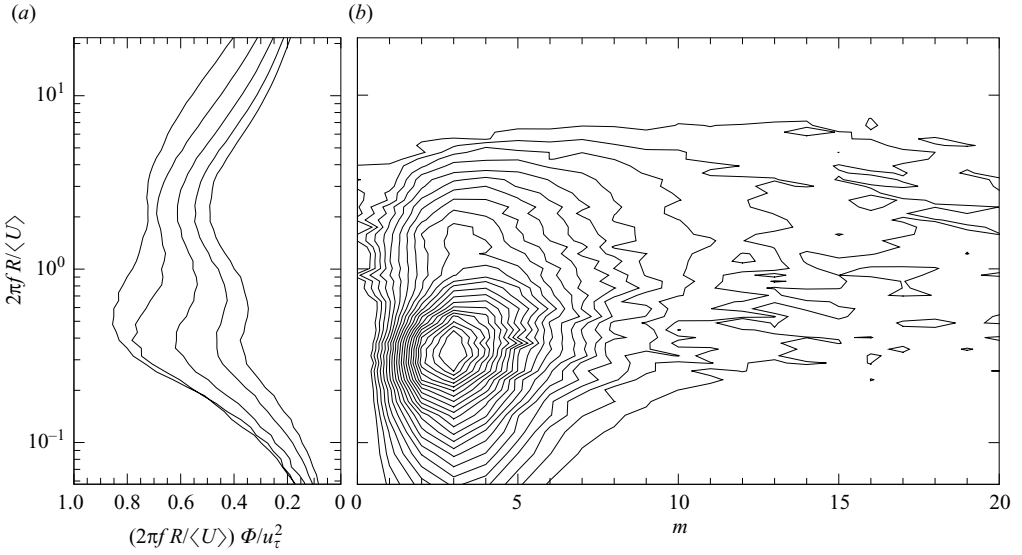

FIGURE 15. Isocontours of pre-multiplied eigenvalues, $(2\pi f/\langle U\rangle)\lambda^{(1)}(m, f)$, distributed across azimuthal modes and normalized frequency, $2\pi f/\langle U\rangle$. Isocontours separated by 2.5×10^{-7} with contours below 5×10^{-7} are not shown for clarity. Autospectra calculated from fixed probe at different wall-normal positions are shown in (*a*) for comparison.

mode 3 at values of $2\pi f R/\langle U\rangle$ corresponding to the VLSM and LSM peaks in the autospectra. The largest values of $\lambda^{(1)}$ are distributed around these peaks, indicating that a large portion of the kinetic energy within the measurement plane is contained within the VLSM and LSM. The majority of energy is contained within the frequency range $2\pi f R/\langle U\rangle < 10$, with the VLSM peak appearing predominantly in the range $2\pi f R/\langle U\rangle < 1$. Thus, these values were used to select the wavenumber ranges applied during spectral filtering (§ 3.3).

When examining the eigenvalue distribution in figure 15, there is no clear delineation between the VLSM and LSM. Nevertheless, the VLSM appear to be concentrated within the lower azimuthal modes (around azimuthal mode 3), which is consistent with the large transverse scales observed in the spectrally filtered results. Conversely, the LSM appear to be distributed over a larger range of azimuthal scales, which suggests that they do not have a dominant transverse scale and are composed of motions encompassing a wide range of streamwise and transverse scales.

The VLSM concentration around azimuthal mode 3 is an interesting result considering the findings of Faisst & Eckhardt (2003), who predict that nonlinear travelling wave instabilities in laminar pipe flow could lead to turbulence transition. They find that travelling waves with threefold azimuthal symmetry are the first to appear with increasing Reynolds number, with additional azimuthal symmetries appearing with increasing Reynolds number. States with up to sixfold symmetry have been observed experimentally by Hof *et al.* (2004). This range appears similar to the range of azimuthal modes observed at VLSM wavenumbers in figure 15, supporting the possibility that the VLSM result from the persistence of unstable travelling waves which form during transition and persist into the turbulent flow regime.

There are several inconsistencies, however, that prevent embracing this mechanism as the VLSM source. First, the travelling waves are expected to form within laminar flow but are themselves inherently unstable, thus it is questionable that these modes could persist in turbulent flow where the mean shear is much different. Second, the wavelengths observed by Faisst & Eckhardt (2003) are much shorter than that of the VLSM (although the wavelength of the instability is Reynolds number and azimuthal mode dependent, generally increasing with higher Reynolds number and decreasing with azimuthal mode). Finally, Faisst & Eckhardt (2003) note a difference between the wavelengths of the travelling waves between pipe and plane Couette flows, but Monty *et al.* (2009) show that the peak in the autospectra corresponding to the VLSM wavelength is strikingly similar for pipes and channels at high Reynolds numbers. Therefore, unless these discrepancies between high Reynolds number turbulent observations of VLSM and observations made at low Reynolds number can be resolved, it would appear unlikely that these phenomena are related, at least for travelling waves of the form reported by Faisst & Eckhardt (2003) and Hof *et al.* (2004).

4. Conclusions

Multi-point, one-component velocity measurements in a smooth-walled pipe flow at $Re_D = 1.5 \times 10^5$ support the hypothesis that the LSM peak observed in the autospectra correspond to the hairpin packet model proposed by Adrian (2007), whereby a packet of hairpin vortices induces a region of uniform momentum, which is inclined to the wall at an angle related to the growth rate of the hairpin packet. Spectrally filtered cross-correlations suggest that in the outer layer these packets are composed of detached eddies which have little correlation with the flow near the wall, and the POD results indicate that they occur across a wide range of azimuthal scales. Within the logarithmic region, it appears more likely that these LSM are attached to the wall. The autospectra certainly suggest that the LSM in the outer layer ($y/R > 0.1$) travel with a common convection velocity which is larger than that of the LSM in the overlap region ($y/R < 0.1$).

The VLSM peak in the autospectra is connected to structures with a large azimuthal scale of approximately one third of the circumference of the pipe, that is, about

one diameter. These structures also have large radial scales which result in a strong correlation with motions near the wall, supporting the hypothesis that these structures are associated with the modulation of the near wall-flow observed by Hutchins & Marusic (2007*b*) and Mathis *et al.* (2009). This larger radial scale also appears to result in the structures becoming stretched to give smaller inclination angles with respect to the wall than what was observed for the LSM, probably due to the increased deformation across these larger radial scales associated with the mean shear.

The lack of clear delineation between the LSM and VLSM in the POD results suggests that these two motions are interrelated. The similarity between the azimuthal scale of the LSM in the outer layer and the VLSM within the overlap layer supports the observation by Bailey *et al.* (2008) that if the VLSM are caused by the streamwise alignment of the LSM, only the LSM in the outer layer are aligning to create these motions. Further evidence for this mechanism can be found in the autospectra which show the increased energy within the LSM compared to the VLSM with increasing distance from the wall, indicating that the detached LSM appear to occur further from the wall than do the VLSM and hence would be above them. In contrast, near the wall, the LSM are attached to the wall, move at a different convection velocity and have much smaller transverse scales than the VLSM, and they are unlikely to be involved in the formation of VLSM.

The support of the Office of Naval Research under grants N00014-07-1-0111 and N00014-09-1-0263 (programme manager Ron Joslin) is gratefully acknowledged.

REFERENCES

Adrian, R. C., Meinhart, C. D. & Tomkins, C. D. 2000 Vortex organization in the outer region of the turbulent boundary layer. *J. Fluid Mech.* **422**, 1–54.

Adrian, R. J. 2007 Hairpin vortex organization in wall turbulence. *Phys. Fluids* **19**, 041301.

Alving, A. E., Smits, A. J. & Watmuff, J. H. 1990 Turbulent boundary layer relaxation from convex curvature. *J. Fluid Mech.* **211**, 529–556.

Bailey, S. C. C., Hultmark, M., Smits, A. J. & Schultz, M. P. 2008 Azimuthal structure of turbulence in high Reynolds number pipe flow. *J. Fluid Mech.* **615**, 121–138.

Balakumar, B. J. & Adrian, R. J. 2007 Large- and very-large-scale motions in channel and boundary-layer flows. *Phil. Trans. R. Soc.* A **365**, 665–681.

Bendat, J. S. & Piersol, A. G. 2000 *Random Data: Analysis and Measurement Procedures*, 3rd edn. Wiley Interscience.

Del Álamo, J. C. & Jiménez, J. 2006 Linear energy amplification in turbulent channels. *J. Fluid Mech.* **559**, 205–213.

Dennis, D. J. C. & Nickels, T. B. 2008 On the limitations of taylor's hypothesis in constructing long structures in a turbulent boundary layer. *J. Fluid Mech.* **614**, 197–206.

Faisst, H. & Eckhardt, B. 2003 Travelling waves in pipe flow. *Phys. Rev. Lett.* **91** (22), 224502.

Favre, A. J., Gaviglio, J. J. & Dumas, R. J. 1957 Space–time double correlations and spectra in a turbulent boundary layer. *J. Fluid Mech.* **2**, 313–342.

Favre, A. J., Gaviglio, J. J. & Dumas, R. J. 1958 Further space–time correlations of velocity in a turbulent boundary layer. *J. Fluid Mech.* **3**, 344–356.

Ganapathisubramani, B., Longmire, E. K. & Marusic, I. 2003 Characteristics of vortex packets in turbulent boundary layers. *J. Fluid Mech.* **478**, 35–46.

Guala, M., Hommema, S. E. & Adrian, R. J. 2006 Large-scale and very-large-scale motions in turbulent pipe flow. *J. Fluid Mech.* **554**, 521–542.

Hof, B., van Doorne, C. W. H., Westerweel, J., Nieuwstadt, F. T. M., Faisst, H., Eckhardt, B., Wedlin, H., Kerswell, R. R. & Waleffe, F. 2004 Experimental observations of nonlinear travelling waves in turbulent pipe flow. *Science* **305**, 1594–1598.

Hoyas, S. & Jiménez, J. 2006 Scaling of the velocity fluctuations in turbulent channels up to $re_\tau = 2003$. *Phys. Fluids* **18** (1), 011702.

Hutchins, N., Hambleton, W. T. & Marusic, I. 2005 Inclined cross-stream stereo particle image velocimetry measurements in turbulent boundary layers. *J. Fluid Mech.* **541**, 21–54.

Hutchins, N. & Marusic, I. 2007*a* Evidence of very long meandering features in the logarithmic region of turbulent boundary layers. *J. Fluid Mech.* **579**, 1–28.

Hutchins, N. & Marusic, I. 2007*b* Large-scale influences in near-wall turbulence. *Phil. Trans. R. Soc.* A **365**, 647–664.

Kim, K. C. & Adrian, R. J. 1999 Very-large-scale motion in the outer layer. *Phys. Fluids* **11** (2), 417–422.

Kovasznay, L. G., Kibens, V. & Blackwelder, R. F. 1970 Large-scale motion in the intermittent region of a turbulent boundary layer. *J. Fluid Mech.* **41** (2), 283–325.

Langelandsvik, L. I., Kunkel, G. J. & Smits, A. J. 2008 Flow in a commercial steel pipe. *J. Fluid Mech.* **595** (1), 323–339.

Marusic, I. & Heuer, W. D. C. 2007 Reynolds number invariance of the structure inclination angle in wall turbulence. *Phys. Rev. Lett.* **99**, 114504.

Mathis, R., Hutchins N. & Marusic, I. 2009 Large-scale amplitude modulation of the small-scale structures in turbulent boundary layers. *J. Fluid Mech.* **628**, 311–337.

McKeon, B. J., Li, J., Jiang, W., Morrison, J. F. & Smits, A. J. 2004 Further observations on the mean velocity distribution in fully developed pipe flow. *J. Fluid Mech.* **501**, 135–147.

Monty, J. P., Hutchins, N., Ng, H. C. H., Marusic, I. & Chong, M. S. 2009 A comparison of turbulent pipe, channel and boundary layer flows. *J. Fluid Mech.* **632**, 431–442.

Monty, J. P., Stewart, J. A., Williams, R. C. & Chong, M. S. 2007 Large-scale features in turbulent pipe and channel flows. *J. Fluid Mech.* **589**, 147–156.

Tavoularis, S. 2005 *Measurement in Fluid Mechanics*. Cambridge University Press.

Tomkins, C. D. & Adrian, R. J. 2003 Spanwise structure and scale growth in turbulent boundary layers. *J. Fluid Mech.* **490**, 37–74.

Tomkins, C. D. & Adrian, R. J. 2005 Energetic spanwise modes in the logarithmic layer of a turbulent boundary layer. *J. Fluid Mech.* **545**, 141–162.

Townsend, A. A. 1976 *The Structure of Turbulent Shear Flow*. Cambridge University Press.

Tutkun, M., George, W. K., Delville, J., Stanislas, M., Johansson, P. B. V., Foucaut, J.-M. & Coudert, S. 2009 Two-point correlations in high Reynolds number flat plate turbulent boundary layers. *J. Turbul.* **10** (21), 1–23.

Tutkun, M., Johansson, P. B. V. & George, W. K. 2008 Three-component vectorial proper orthogonal decomposition of axisymmetric wake behind a disk. *AIAA J.* **46** (5), 1118–1134.

Zagarola, M. V. 1996 Mean-flow scaling of turbulent pipe flow. PhD thesis, Princeton University.

Zagarola, M. V. & Smits, A. J. 1998 Mean-flow scaling of turbulent pipe flow. *J. Fluid Mech.* **373**, 33–79.

Zhou, J., Adrian, R. J., Balachandar, S. & Kendall, T. M. 1999 Mechanisms for generating coherent packets of hairpin vortices in channel flows. *J. Fluid Mech.* **387**, 353–396.